Near-Field Spectroscopy of the Quantum Constituents of a Luminescent System

H. F. Hess, E. Betzig, T. D. Harris, L. N. Pfeiffer, K. W. West

Luminescent centers with sharp (<0.07 millielectron volt), spectrally distinct emission lines were imaged in a GaAs/AlGaAs quantum well by means of low-temperature near-field scanning optical microscopy. Temperature, magnetic field, and linewidth measurements establish that these centers arise from excitons laterally localized at interface fluctuations. For sufficiently narrow wells, virtually all emission originates from such centers. Near-field microscopy/spectroscopy provides a means to access energies and homogeneous line widths for the individual eigenstates of these centers, and thus opens a rich area of physics involving quantum resolved systems.

The energetics of two-dimensional systems is an active area of research in disciplines ranging from biology to physics. Examples include light-harvesting complexes in plants, self-assembled molecular layers, and the fractional quantum Hall effect. The unique character of these systems is that a plane rather than a volume of states determines the essential optical and electrical properties. One tool frequently used to explore these properties is photoluminescence (PL) spectroscopy. However, the measurements of energy levels, transport length scales, and relaxation times obtained in this manner are averaged values of a larger, possibly nonstatistical distribution reflecting intrinsic inhomogeneities between different emission sites as well as additional inhomogeneities arising from local environmental perturbations. The opportunity for important insight is often lost by the inability to resolve details within this distribution. Spectroscopy based on the near-field scanning optical microscope (NSOM) (*1*), with its subwavelength spatial resolution, offers promise to probe beyond this limitation and attain the ultimate goal of resolving and characterizing the individual optically active quantum emitters in such planar systems.

One important example of an artificial two-dimensional system is the quantum well heterostructure, in which a thin (~100 Å) sheet of low band gap (energy) semiconductor material is clad on either side by higher band gap material, confining the excitation to a plane. Such structures are employed in many technologically important semiconductor devices such as quantum well lasers and high electron mobility transistors. The performance of such devices is influenced by interface roughness, impurity concentration, and alloy homogeneity of the quantum well. Here too, PL spectroscopy (*2*) has proven to be a powerful diagnostic tool, but PL has shown its limitations arising from the spatial averaging of spectral information. Partly as a result of these limitations, a plethora of techniques have been enlisted in the study of single quantum well structures (SQWs), including cathodoluminescence (*3*), scanning tunneling microscopy (STM) (*4, 5*), and transmission electron microscopy (TEM) (*6*). Although much insight has been generated by these techniques, so has considerable controversy, as each has resulted in a different picture of the microscopic structure within SQWs. Part of this apparent disagreement stems from the difference in length scales probed by each technique (*7*). As NSOM accesses the 10-μm to 0.1-μm range intermediate to conventional PL and TEM/STM, it has the potential to bridge the gap in interpretation between these methods, thereby leading to a relatively complete understanding of the SQW structure on all length scales while at the same time revealing the true origin of the luminescence.

Near-field photoluminescence microscopy/spectroscopy. To fully exploit this potential, near-field microscopy/spectroscopy is most advantageously performed at cryogenic temperatures (*8*), so that the high spatial resolution inherent in NSOM is coupled with the high spectral resolution and high quantum efficiency obtainable when thermal broadening and nonradiative recombination are minimized. Consequently the low temperature near-field system outlined in Fig. 1 was constructed. In brief, light from a tunable dye laser at excitation wavelength λ_{exc} was coupled into a tapered, aluminum-coated optical fiber having a subwavelength diameter aperture at its apex (*9*). After positioning this probe to <20 nm from the sample (*10*), photons emitted from the aperture and absorbed in the sample created electrostatically bound electrode hole pairs (excitons) which migrated in the plane of the quantum well prior to recombination. The resultant luminescence was collected on the same side of the sample with a lens and transported via an optical fiber bundle to a 0.5-m spectrometer with a cooled charge-coupled device (CCD) camera for detection.

For these initial experiments, the primary sample was grown by molecular beam epitaxy (MBE) and consisted of four $GaAs/Al_{0.32}Ga_{0.68}As$ SQWs of thicknesses 31 Å, 23 Å, 45 Å, and 90 Å, each separated by 250 Å barriers and centered at depths of 266 Å, 542 Å, 826 Å, and 1144 Å, respectively. To enhance the formation of smooth interfaces, the sample was grown at 610°C with interruptions of 60 s and 30 s at the GaAs and $Al_xGa_{1-x}As$ surfaces, respectively (*11*). The high quality of the sample was attested by a low impurity concentration of $<10^{15}$ cm^{-3} (as determined by far-field PL on the underlying GaAs

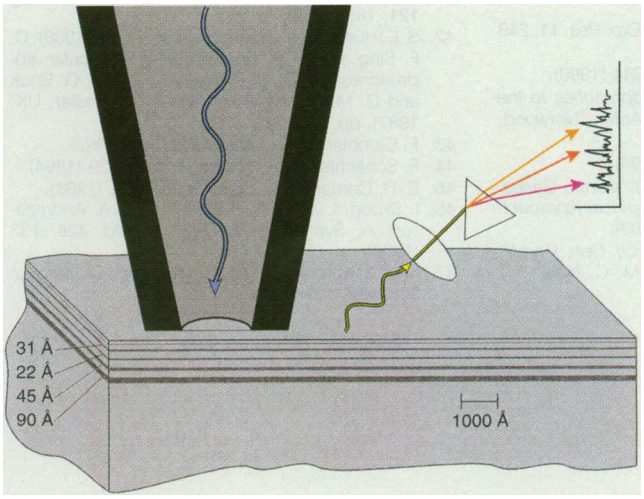

Fig. 1. Cutaway schematic of the illumination and collection geometry used for near-field PL microscopy/spectroscopy. The probe and the sample portions are drawn to scale.

The authors are at AT&T Bell Laboratories, 600 Mountain Avenue, Murray Hill, NJ 07974, USA.

epilayer) and by mobilities of $\sim 2 \times 10^6$ cm^2 V^{-1} s^{-1} measured on other heterostructures grown in the same MBE system shortly thereafter.

Spatial variations in the PL spectrum were measured by raster scanning the sample laterally under the near-field probe in the plane of the SQWs with a scan head operating in vacuum that was surrounded by an 8-T superconducting magnet and immersed in liquid helium. The luminescence intensity was recorded as a function of the emission wavelength λ and the spatial coordinates x and y, resulting in the data set $L(\lambda,x,y)$. Any one variable of the set could be fixed to extract a conventional image $L(x,y)|_\lambda$ at a given luminescence wavelength, or images $L(\lambda,x)|_y$ or $L(\lambda,y)|_x$ of spectral evolution with linear position (*12*).

Spectral features in the near field. Several such images from one data set (thickness = 23 Å, λ_{exc} = 694 nm, T = 2 K) are shown in Fig. 2. A typical near-field spectrum $L(\lambda)|_{x\,=\,5.1\ \mu m,\ y\,=\,4.1\ \mu m}$ (solid line, top) taken at the center pixel of the 1-μm box shown at bottom differs markedly from a conventional far-field spectrum $L(\lambda)_{FF}$ (dashed line, top) of the same quantum well. The near-field spectrum evolves rapidly with position [demonstrated in $L(\lambda,x)|_{y\,=\,4.1\ \mu m}$, Fig. 2 center], but the average of all near-field spectra $\langle L(\lambda)\rangle_{NF}$ over the 6.4 μm × 6.4-μm scan area (Fig. 2, top, colored line) closely approximates $L(\lambda)_{FF}$. Furthermore, images $L(x,y)|_\lambda$ at several λ (Fig. 2, bottom), demonstrate that the unusually sharp spectral features in the near-field data are also highly localized in space. Thus, we reveal discrete luminescence sites of well-defined energy that spatially average to form the inhomogeneously broadened far-field spectra traditionally observed from such narrow wells. This is analogous to the situation found in low-temperature far-field spectroscopy of fluorescent molecules, where the individual molecular constituents of an inhomogeneously broadened ensemble are spectrally resolved when doped at sufficiently low density within a host crystal (*13*). In our case, however, the individual luminescent centers are not resolved by their low density, but rather by the combination of high spatial and spectral resolution within our near-field system.

The areal density of luminescent sites can be estimated as follows. At the spatial resolution of our instrument there are ~30 spectrally resolved lines at any given position. That not all these lines originate from the same site is evident from the images A, C, and D corresponding to the labeled spectral peaks. Here different spatial luminescence patterns overlap. However, in other cases, identical luminescence patterns can be identified for several different spectral peaks such as the pair B and C. These might arise from different quantum eigenstates of the same site, but non-overlapping closely spaced (<1000 Å) eigenstates from unresolved yet distinct sites

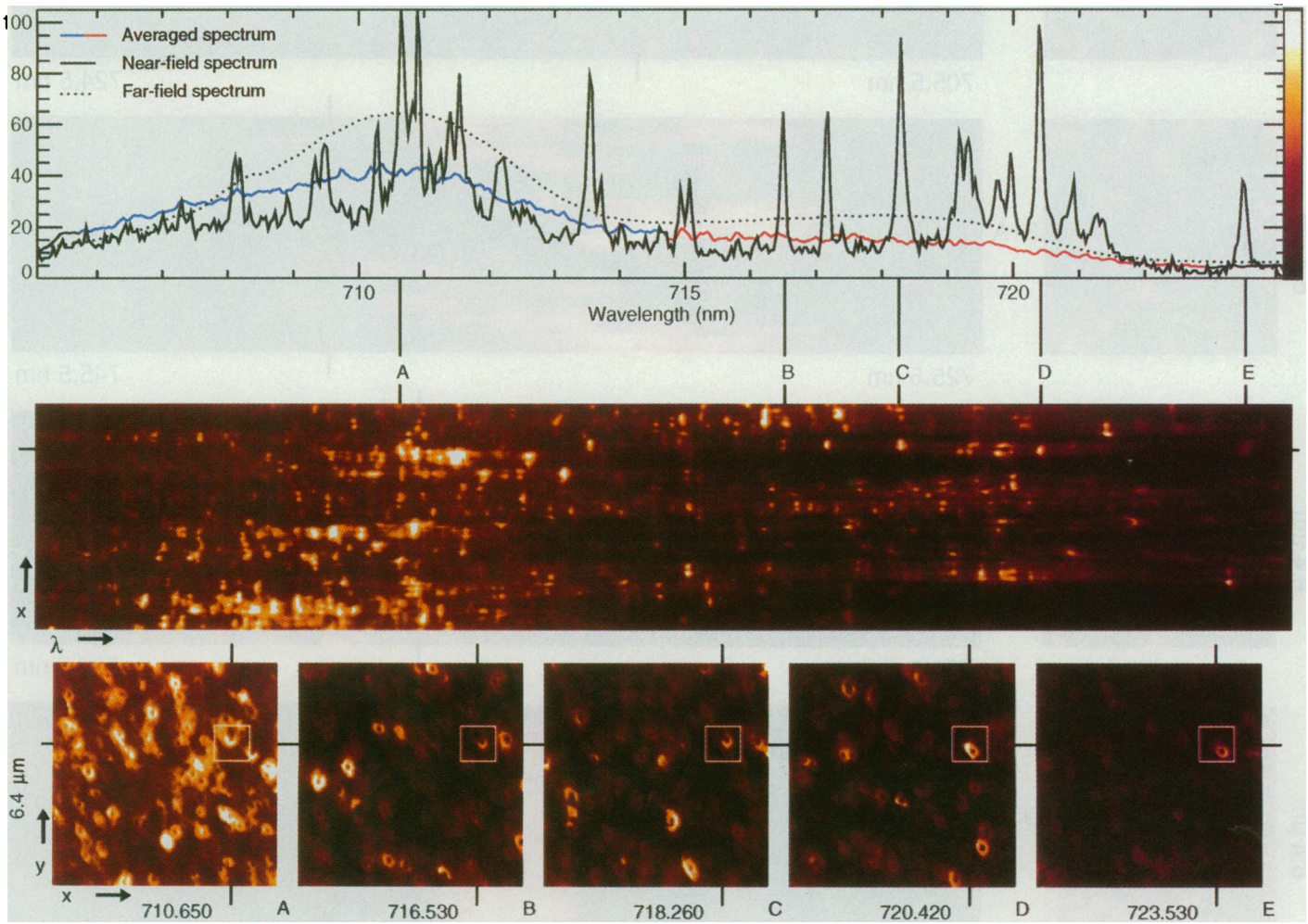

Fig. 2. (**Top**) Near-field, far-field, and spatially averaged near-field PL spectra from a 23 Å SQW produced with 696-nm excitation at 2 K. (**Middle**) Spatial evolution of the near-field spectrum with linear position, presented as the image $L(\lambda,x)|_y$. (**Bottom**) Real space near-field images $L(x,y)|_\lambda$ at the five wavelengths labeled above. Luminescence is found to originate from only certain spatially and spectrally discrete sites, which appear as rings. The tick marks around each image indicate the x, y coordinates where the near-field spectrum at top was taken as well as the line along which the spectral evolution in the middle was recorded.

cannot be ruled out. Depending on this last assumption there are about 30 to 300 sites μm^{-2} in the 23 Å SQW. This density is not strongly influenced by well thickness (for thickness <50 Å), sample growth conditions (*14*), excitation wavelength (from 670 nm to 699 nm in the 23 Å SQW), or polarization. It is, however, at least an order of magnitude greater than the areal density of impurities (<2 μm^{-2}) deduced from the aforementioned epilayer measurements, thus demonstrating that the majority of the luminescent sites originate from some other source.

The possible effects of heating by the probe and high intensity illumination were also carefully considered. Although the density of sites was temperature invariant up to 15 K, the distribution of luminescence intensity between sites changed noticeably even when the temperature was raised from only 2 K to 3 K. Furthermore, the luminescence intensity varied linearly when the excitation was cut in half. Finally, although the excitation intensity of ~35 W cm^{-2} extrapolated at the aperture was large compared with most conventional PL measurements, the illuminated area was so small and the absorption within the SQWs so slight that at most only a single exciton was present at any one time (*15*). At substantially greater power levels, probe heating will become a serious problem, yet nonlinear spectroscopy with pulsed excitation remains a possibility, as long as the average power coupled into the probe stays comparable to the ~1 mW used here.

Migration and trapping of excitons. The picture that emerges from Fig. 2 is one in which the potential energy surface in the plane of the SQW is deeply corrugated. Each exciton created locally travels only a short distance before being captured by a local potential minimum, where it eventually recombines. The resulting luminescent centers appear as rings rather than as dots because their emission is occluded when each is directly under the near-field probe.

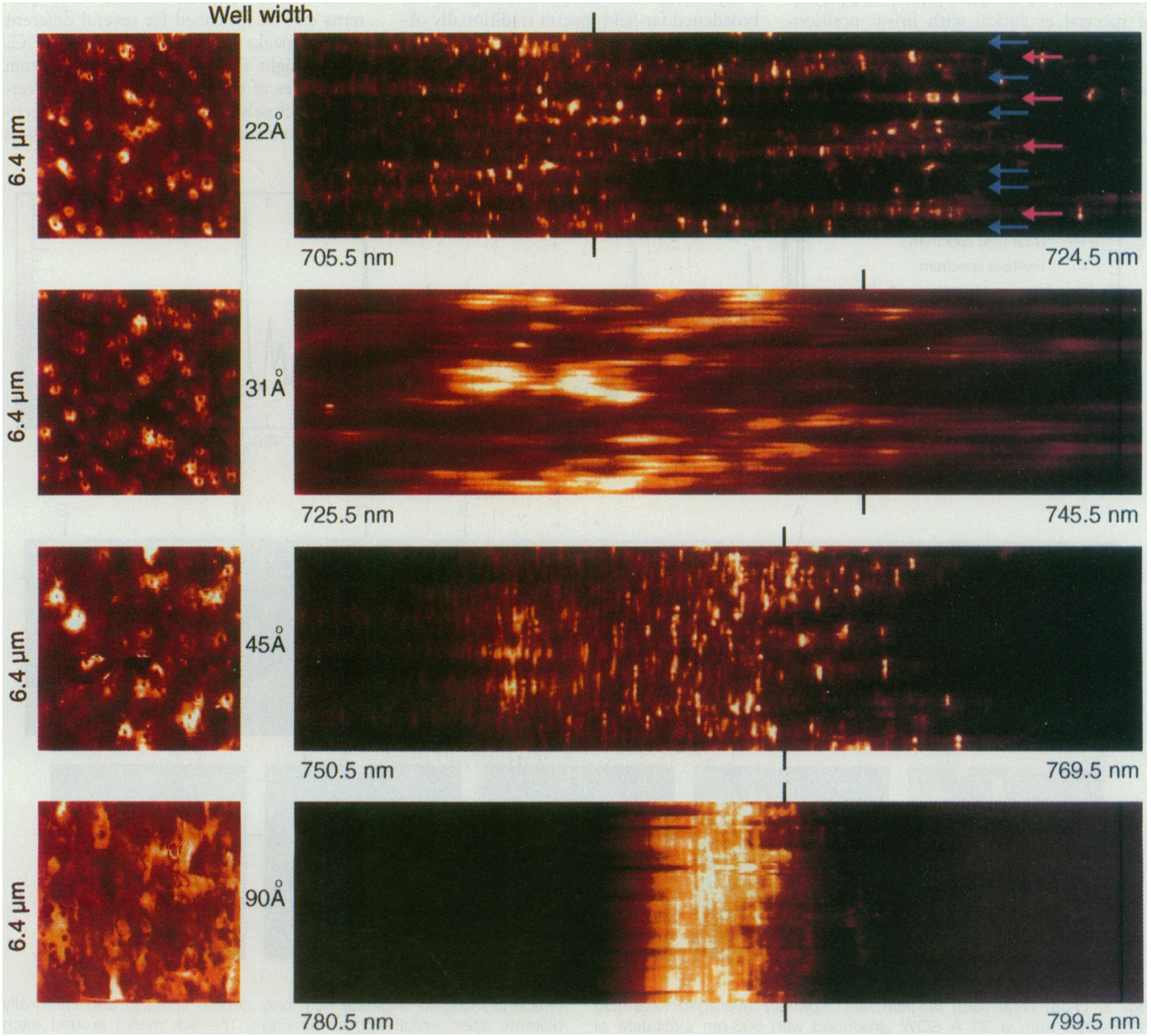

Fig. 3. Real space $L(x,y)|_\lambda$ (**left**) and spectral evolution $L(\lambda,x)|_y$ images (**right**) of luminescence centers in four SQWs of differing thickness. The tick marks on the spectral evolution images indicate the wavelength of the neighboring real space images. Blue and red arrows highlight the signature of monolayer fluctuations in the 23 Å SQW.

Consequently, the brightness of each ring reflects not only the oscillator strength of the associated minimum, but also the local diffusion length (δ) to reach the minimum. Likewise the size and shape of each ring provides information on the scale and asymmetry of diffusion around the minimum.

Overall, δ should depend upon both the depth and density of the potential energy minima as well as temperature. The depth of the minima can be controlled by varying the well thickness, as is explored for the four SQWs in Fig. 3. The gradual increase in the ring radius from ~1500 Å to ~2500 Å seen between the 31 Å and 45 Å SQWs in the $L(x,y)|_\lambda$ images at left and the more pronounced spreading evident between the 45 Å and the 90 Å wells reflect the longer diffusion allowed by reduced exciton scattering and trapping from the smaller corrugation potential in these thicker wells (*16*). No further spreading was apparent in raising the temperature from 2 K to 14 K, the only observed effect being a change in the relative intensity of the various centers with an overall brightening of lower energy centers. This is consistent with far-field PL measurements and reflect the higher probability that an exciton can thermally escape to a deeper potential minimum nearby. A complete microscopic picture of exciton migration (*17*) by phonon assistance, tunneling, or ballistic propagation can now be experimentally established on the basis of the spatial luminescence shapes, intensities, and energies as well as their temperature dependence.

The spectral consequences of decreasing well thickness are shown in the $L(\lambda,x)|_y$ images at right of Fig. 3. Overall the emission lines shift to higher energy and simultaneously broaden their distribution. Related behavior is seen in the far-field peak, where the broadening has been interpreted as evidence of the increasing influence of local well thickness fluctuations as the well becomes ever narrower (*18*). As applied to the near-field data, this suggests that local regions of slightly greater well thickness are the source of potential energy minima which trap excitons and thereby give rise to local emission, a hypothesis explored in more depth below.

Characterization of the individual eigenstates. Perhaps most significant is that the majority of the emission lines are so narrow (at or beyond the 0.07 meV resolution limit of our spectrometer) that, together with the lateral size constraints on the centers, we can identify each such line as arising from an individual three dimensionally confined quantum state. To be specific, the spatial resolution of ~1000 Å places an upper bound on the confinement volume of each site, resulting in a separation of at least 1 meV between the lowest energy eigenstates, or well within the spectral resolution of our system. In addition, such narrow lines: (i) place a lower bound of 60 ps on the lifetime; (ii) are consistent with homogeneous linewidths deduced by other techniques (*19, 20*); and (iii) underscore the localized nature of the emission, because free excitons have larger linewidths of 0.22 meV (*21*). With higher spectral resolution measurements of linewidths and energies, details such as the shape and depth of the potential minima (*22*) as well as the dynamics (*17, 23*) of each constituent eigenstate might be deduced.

One exception to this general picture is the 31 Å SQW nearest the surface (with depth 265 Å), where although the emission sites remain spatially localized, their energies are broadened by ~2 meV. This may result from migrating surface charges which could introduce time varying local potentials by their electrostatic fields (*24*). Since this effect is no longer noticeable in the 23 Å SQW at a depth of 542 Å, it has a finite range. Quantum wells designated to take advantage of the highest near-field resolution need to be within this range and thus risk similar spectral broadening.

Further evidence that the corrugated potential energy environment experienced by an exciton is dominated by well thickness fluctuations and not impurities comes from the magnetic field (B_z) dependence of the near-field spectra. The images $L(\lambda,B_z)|_{x,y}$ at the upper left and right of Fig. 4 display the spectral evolution with B_z at specific points on the 23 Å and 45 Å SQWs, respectively. The vast majority of the energy levels split linearly with B_z at 85 μeV T^{-1} into two states. This is consistent with excitons confined by local well thickness fluctuations (*25*), where only the spin states $|S^e_z = +1/2, J^{hh}_z = -3/2\rangle$ and $|S^e_z = -1/2, J^{hh}_z = +3/2\rangle$ of the electron and heavy hole pair allow recombination. In contrast, impurity bound excitons can be expected to yield more complicated splittings introduced by the additional spin states of the impurity. One such splitting (a possible triplet) is shown at a different point in the case of the 23 Å SQW (Fig. 4A). However, such splittings were extremely rare and may only represent a case of overlapping doublets.

Also apparent in the upper two images of Fig. 4 is a quadratic diamagnetic shift of each doublet to higher energy. This shift varies from 13 μeV T^{-2} in the 23 Å well to 16 μeV T^{-2} in the 45 Å well. This small shift confirms the excitonic nature of the emission, as free carrier recombination with a neutral impurity should display a stronger diamagnetic dependence. Quadratic diamagnetic shifts of comparable magnitude have been observed as well from the broadened peaks of far-field PL (*26*), but near-

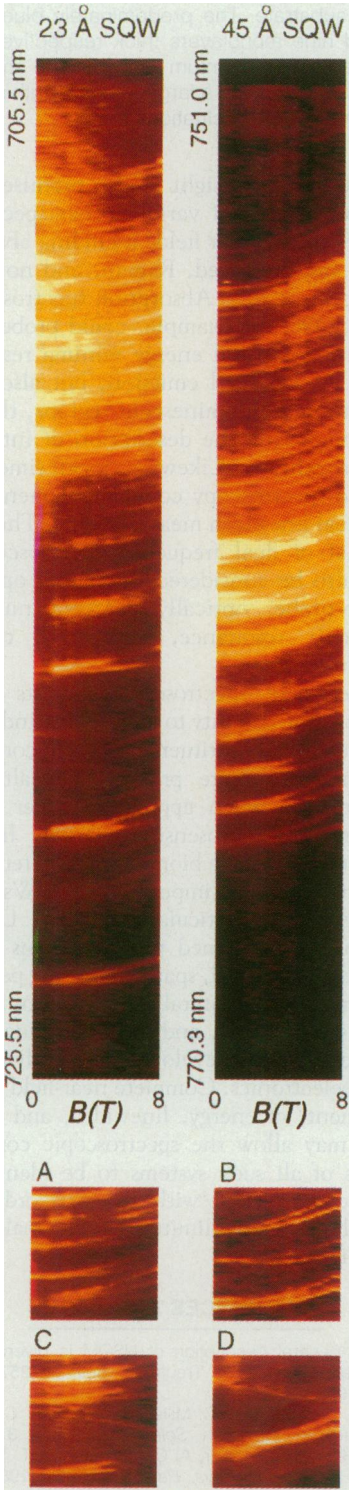

Fig. 4. (**Top**) Images $L(\lambda,B_z)$ of the evolution of the near-field spectrum with increasing magnetic field, at specific points on the 23 Å (**left**) and 45 Å (**right**) SQWs. The magnitude of the diamagnetic shift and the pairwise splitting of each line provide evidence that the emission arises from localized excitons. Anomalous behavior observed for certain rare eigenstates include: (**A**) a possible triplet splitting; (**B**) differing diamagnetic dependences; and (**C** and **D**) paramagnetic shifts to lower energy.

field measurements are required to reveal subtle differences in the shift from one luminescent state or site to another. For example, occasional yet noticeable variations in the quadratic diamagnetic coefficient (Fig. 4B, 45 Å SQW) may reflect differences in the lateral confinement energy arising from the local interface roughness (that is, quantum box effect). In other rare instances, the spectral features shift to lower energy with increasing B_z (Fig. 5, C and D). This may be indicative of an additional splitting from an exciton bound to a single impurity, or it may be the signature of an excited state of a single roughness induced potential minimum.

Interfacial quality. Another signature of well thickness fluctuations is found in the multiple far-field emission peaks associated with each SQW. Such structure is traditionally ascribed to islands of differing monolayer thickness within each well. In the near field, it is manifested as a series of spatially resolvable regions in which the spectral distribution of emission lines shifts abruptly up or down in energy by an amount approximately consistent with a monolayer change in confinement energy. The red and blue arrows at the top right of Fig. 3 highlight where the average luminescence has shifted to the red or blue end of the spectrum for the 23 Å SQW. To form a spatial map of these islands, the three-dimensional near-field data set $L(\lambda,x,y)$ for the 23 Å SQW was spectrally integrated to determine separately the local average wavelength and the local luminescence intensity. The average wavelength spans a 10-nm range about 713 nm and is mapped onto hue of the visible spectrum to form the composite image of Fig. 5A, where brightness is scaled by the luminescence intensity. Regions of different monolayer thickness such as blue regions and the yellow/pink regions are readily apparent and map onto the corresponding blue and neighboring red peak in $\langle L(\lambda)\rangle_{NF}$ in Fig. 1, top. The features also display a $0\bar{1}1$ orientation consistent with elongated islands observed in STM measurements on homoepitaxially grown GaAs (4). Using the same color and intensity mapping (except now centered at 733 nm instead of 713 nm), very similar hue patterns are observed on other SQWs from the same sample such as the 31 Å well shown in Fig. 5B. Since the same area is scanned for both images, one can see that the thick and thin regions of the quantum wells are remarkably well correlated. In fact, the locations of greatest thickness correspond very well to depressions on the sample surface, as determined from the simultaneously generated near-field reflectivity image and independent profilometry (which yields typical depths of ~30 Å). The tendency of each depression to be partially filled in by successive GaAs layers explains this correlation. In contrast, a 27 Å SQW grown on a different sample without interruptions and at a higher temperature of 650°C displays much smaller and more gradual wavelength (that is, hue) variations (Fig. 5C, spectral center of 704 nm). This visually indicates how higher growth temperatures suppress the formation of large-scale regions of monolayer fluctuations while maintaining the smaller scale fluctuations responsible for localizing the exciton. The three images demonstrate that monolayer fluctuations in thickness of a SQW can be inferred on a variety of lateral length scales, ranging from islands of up to micron dimensions, down through the spatial resolution limit of 1000 Å, and beyond to the exciton confinement size of ~50 Å implied by the spectral distribution of the individual quantum eigenstates. Thus, our results not only provide a bridge between the measurements of STM/TEM and far-field PL but also can serve as a useful diagnostic for determining interfacial quality in heterostructures.

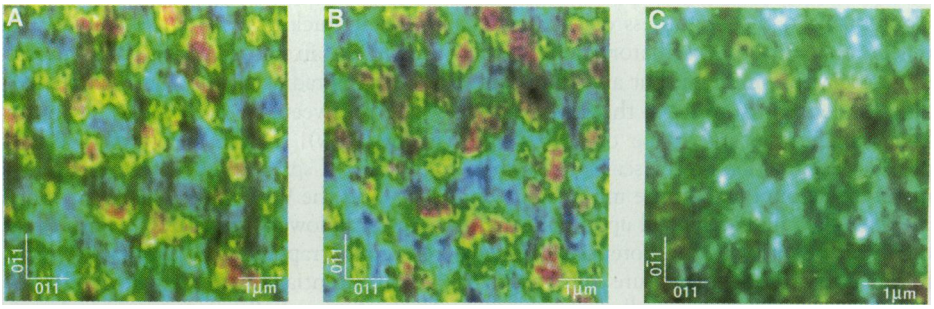

Fig. 5. Composite color near-field images of luminescence from: (**A**) a 23 Å SQW, grown at 610°C; (**B**) a 31 Å SQW from the same sample, with growth conditions and scan area the same as in (A); and (**C**) a 27 Å SQW, grown at 650°C on a different substrate. The predominately blue and yellow/pink regions in (A) represent islands eight and nine monolayers thick respectively. A similar pattern of thickness fluctuations exists for the adjoining quantum well (B). The smaller range of hues in (C) indicates that full monolayer fluctuations on such a large lateral length scale are absent for higher growth temperatures, although small scale fluctuations remain.

Future prospects. Near-field spectroscopy offers unique attributes in addition to high spatial resolution which might be exploited in future experiments. In particular new optical transitions ordinarily forbidden in far-field spectroscopy may now become allowed (27). For example, the presence of high lateral spatial frequency optical fields allow access to k-vectors that could be used to map dispersion relationships more completely. The existence of significant longitudinal field components might also result in new optical selection rules. Indeed, knowledge of the complete electromagnetic field distribution in the vicinity of the subwavelength aperture could be used to identify the direction and oscillator strength of individual dipolar transitions of the SQW, in analogy to recent experiments involving single fluorescent molecules (28).

Additional insight is also promised by the adaptation of various other spectroscopies to the near field, including absorption, time resolved, Raman, and nonlinear spectroscopy. Absorption spectroscopy of a SQW, for example, could probe not just the potential energy minima responsible for localized emission, but also the remaining nonluminescent regions, thereby completing the description of interfacial roughness. Likewise, local time resolved spectroscopy could supplement individual linewidth measurements. The full arsenal of dual frequency spectroscopies can also be considered, including optical pump-probe, optically detected nuclear magnetic resonance, and Stark tuned spectroscopy.

Near-field spectroscopy and its now demonstrated ability to identify the individual quantum constituents of a semiconductor heterostructure promise a wealth of information when applied to other two-dimensional photosensitive systems. Investigations of planar biomolecular systems or individual atomic impurities in SQWs may prove to be particularly fruitful. Lithographically patterned planar systems with artificially induced, spatially varying perturbations are also natural candidates for near-field spectroscopy, and are of considerable interest in the development of advanced microelectronics. Complete near-field measurements of energy, linewidth, and position may allow the spectroscopic components of all such systems to be identified and characterized with the extraordinary detail previously limited to the realm of atomic physics.

REFERENCES AND NOTES

1. A general description of NSOM is given in E. Betzig and J. K. Trautman, *Science* **257**, 189 (1992).
2. C. Weisbuch, R. C. Miller, R. Dingle, A. C. Gossard, W. Wiegman, *Solid State Comm.* **37**, 219 (1981); R. C. Miller, A. C. Gossard, W. T. Tsang, O. Monteanu, *Phys. Rev. B* **2**, 3871 (1982); T.

Fukunaga, K. L. I. Kobayashi, H. Nakashima, *Surf. Sci.* **174**, 71 (1986). See also the review in M. A. Herman, D. A. Bimberg, J. Christen, *J. Appl. Phys.* **70**, R1 (1991).
3. J. Christen, M. Grundmann, D. Bimberg, *J. Vac. Sci. Technol.* **B9**, 2358 (1991); C. A. Warwick and R. Kopf, *Appl. Phys. Lett.* **60**, 386 (1992).
4. J. Sudijono, M. D. Johnson, C. W. Snyder, M. B. Elowitz, B. G. Orr, *Phys. Rev. Lett.* **69**, 2811 (1992).
5. R. F. Kopf, E. F. Schubert, T. D. Harris, R. S. Becker, G. H. Gilmar, *J. Appl. Phys.* **74**, 6139 (1993).
6. A. Ourmazd, D. W. Taylor, J. Cunningham, *Phys. Rev. Lett.* **62**, 933 (1989).
7. C. A. Warwick, W. Y. Jan, A. Ourmazd, T. D. Harris, *Appl. Phys. Lett.* **56**, 2666 (1990).
8. R. D. Grober *et al.*, *Appl. Phys. Lett.* **64**, 1421 (1994); R. D. Grober, T. D. Harris, J. K. Trautman, E. Betzig, *Rev. Sci. Instrum.* **65**, 626 (1994).
9. E. Betzig, J. K. Trautman, T. D. Harris, J. S. Weiner, R. L. Kostelak, *Science* **251**, 1468 (1991).
10. Shear force feedback [E. Betzig, P. L. Finn, J. S. Weiner, *Appl. Phys. Lett.* **60**, 2484 (1992)] was used to locate the surface, but disabled during PL scanning.
11. D. Gammon, B. V. Shanabrook, D. S. Katzer, *ibid.* **57**, 2710 (1990).
12. The size of a typical data set $L(\lambda,x,y)$ was 578 × 128 × 128 pixels, covering a range of 20.6 nm × 6.4 μm × 6.4 μm. Peak signals from individual spectral features were of order 10^2 counts in a 1-s integration time, yielding a total scan time of ~7 hours. Trade offs between signal strength and spatial resolution led to the choice of a 1700 Å diameter aperture, resulting in an intrinsic near-field resolution of ~1000 Å. The excitation power transmitted through this aperture was estimated at ~10 nW (~3.6×10^{10} photons s^{-1} @ λ_{exc} = 720 nm). The excitation wavelength was set typically 10 nm below the bottom of the recorded spectral range.
13. W. E. Moerner and L. Kador, *Phys. Rev. Lett.* **62**, 2535 (1989); M. Orrit and J. Bernard, *ibid.* **65**, 2716 (1990).
14. Similar spectral and spatial signatures were observed on a different sample grown at 650°C, a temperature better suited for optimal transport properties.
15. Assuming 1% absorption in a SQW, an exciton was created on average only every 3 ns. Since the exciton lifetime is ≤1 ns, radiative recombination and thermal relaxation of the lattice was completed well before the next absorption event.
16. In estimating δ, the depth dependent near-field resolution must also be considered, but with the exception of the 23 Å SQW of 542 Å depth for which δ is smallest, the SQWs are sufficiently close to the surface and the refractive index is sufficiently high that the intrinsic resolution is small on the scale of δ.
17. T. Takagahara, *Phys. Rev. B* **31**, 6552 (1985).
18. D. C. Reynolds *et al.*, *Appl. Phys. Lett.* **46**, 51 (1985); J. Singh, K. K. Bajaj, C. Chaudhuri, *ibid.* **44**, 805 (1984).
19. J. Hegarty, M. D. Sturge, C. Weisbuch, A. C. Gossard, W. Wiegamann, *Phys. Rev. Lett.* **49**, 930 (1982).
20. H. Wang, M. Jiang, D. G. Steel, *ibid.* **65**, 1255 (1990).
21. A. Vinatteri *et al.*, *Solid State Commun.* **88**, 189 (1993); V. Scinivas, J. Hryniewics, Y. J. Chen, C. E. C. Wood, *Phys. Rev. B* **46**, 10193 (1992).
22. V. Halonen, T. Chakraborty, P. Pietilaeinen, *Phys. Rev. B* **45**, 5980 (1992).
23. D. S. Citrin, *ibid.* **47**, 3832 (1993).
24. D. A. B. Miller *et al.*, *ibid.* **32**, 1043 (1985).
25. Q. X. Zhao and T. Westgaard, *ibid.* **44**, 3726 (1991).
26. M. Potemski *et al.*, *ibid.* **43**, 14707 (1991); D. C. Rogers, J. Singleton, R. J. Nicholasm, C. T. Foxon, K. Woodbridge, *ibid.* **34**, 4002 (1986).
27. R. Grober and T. D. Harris, paper presented at the Second International Conference on Near-Field Optics, Raleigh, NC, 20 to 22 October 1993; R. Grober and T. D. Harris, preprint.
28. E. Betzig and R. J. Chichester, *Science* **262**, 1422 (1993).
29. The authors gratefully acknowledge the contributions of U. Mohideen, R. Chichester, R. Ruel, H. Stormer, A. Pinczuk, J. Shah, J. Stark, and M. Ferarri.

10 March 1994; accepted 6 May 1994